DOI: 10.13009/EUCASS2022-6149
9TH EUROPEAN CONFERENCE FOR AERONAUTICS AND SPACE SCIENCES (EUCASS)

Advanced Guidance Approach for Multi-Body/Multi-Actuator Spacecraft Repointing under Attitude Constraints

Alison Ponche[⋆†], *Andrés Marcos*[⋆], *Thomas Ott*[⋆⋆], *Ramin Geshnizjani*[⋆⋆], *and Johannes Loehr*[⋆⋆]

[⋆]*University Carlos III de Madrid (UC3M)*
Juan Benet Building, Av. de la Universidad 30, 28911, Leganes, Spain
aponche@pa.uc3m.es · anmarcos@ing.uc3m.es

[⋆⋆]*Airbus Defence and Space GmbH*
Claude-Dornier-Strasse 1, 88090 Immenstaad, Germany
thomas.ott/ramin.geshnizjani/johannes.loehr@airbus.com

[†]Corresponding author

Abstract

Current and future space observation missions need to perform many large-angle, multi-axis slew maneuvers between the observations while keeping the attitude in a safe region. The state-of-practice typically divides the multi-axis maneuver into a series of single-axis sub-maneuvers. This ensures that the constraints are explicitly considered and results in simple on-board algorithms' implementation, but is time-consuming and non-optimal for the whole multi-axis maneuver. This article proposes a novel analytical guidance approach which uses the full spacecraft maneuvering capacity and relies on the convexity of the permissible attitude zone. The proposed guidance is time-optimal for a given spacecraft design and set of observation targets. The reduction of slew time is assessed on a multi-body/multi-actuator benchmark spacecraft, whose complex repointing phase requires an autonomous on-board guidance computation. It is shown that the approach is systematic and the reduction of maneuver time considerable.

1. Introduction

Observation spacecraft need to perform many (>1500 per year) large angle and precise attitude slew maneuvers between the observations while satisfying safety critical attitude constraints. For space telescopes, the attitude constraints are due to the thermal high sensitivity of the scientific instruments, and the necessity to prevent sunlight from entering their field of view.[3,6,7,33,38] For Sun observation spacecraft, the heat shields shall maintain an accurate pointing at the Sun throughout all scenarios for them to stay within their thermal limits.[12,36] These attitude exclusion zones are hard constraints, and their violation could lead to the loss of the missions.

Moreover, these missions aim to improve the scientific return by maximizing the image quality and resolution. This is achieved by augmenting the telescope's objective aperture, and thus its focal length. This leads to designing massive space observatories. To further improve the scientific performance, new space observation missions rely on the use of multi-body and multi-actuator (MB/MA) spacecraft architectures. They enable to observe the same target successively with different on-board instruments by using a common movable focusing device. But the trade-off from this higher scientific return is that these types of MB/MA space systems represent a challenge for attitude control design. Indeed, the repointing of such spacecraft involves a focusing device steering towards the line-of-sight (LoS) of the observing instrument plus a spacecraft slew maneuver. This requires to correctly set the initial attitude conditions for the slew maneuver after the mirror motion, which in turn requires to know in real time the spacecraft attitude.

There are two main types of scientific observations: planned and unplanned. For the former, it is important to maximize the time availability during the mission life-time. The latter arise when spontaneous and time-finite events occur and it is scientifically advantageous to observe them. These observations may require to slew very quickly, and thus, the minimization of the time spent re-orienting the spacecraft is a main driver. Performing autonomous slew maneuvers with attitude constraints requires computational efficient motion planning algorithms that can be run on-board in finite time. Currently, there are no efficient and simple optimal solutions in the literature for such a MB/MA scientific observation space mission. This article addresses the aforementioned needs and presents an advanced guidance strategy for reorienting autonomously space observation spacecraft under Sun avoidance and attitude actuator constraints.

DOI: 10.13009/EUCASS2022-6149

The article is organized as follows. After a comparison of industrial technical concepts for observation missions, section 2 presents a benchmark mission together with the definition of its guidance problem. A reaction wheel equipment and configuration are proposed and the spacecraft angular momentum and torque capacity is formulated. Then, a reference repointing guidance between two observations is proposed in section 3. It is based on an industrial state-of-practice slew guidance that satisfies attitude constraints. Then, a novel slew maneuver guidance approach, developed to minimize maneuver time, is formulated in section 4. Both approaches are finally compared and the reduction of maneuver time achieved with the proposed approach is shown. The assessment includes evaluation by Airbus team, on an in-house Space observation MB/MA simulator, of the gains of the approach.

2. Space observation benchmark mission

In this section, the industrial technical concepts for current and future space observation missions are investigated. Based on this study, a benchmark observation mission is considered, and a guidance problem is formulated. Then, a method to assess the maneuver performance and compare the guidance approaches is presented.

2.1 Comparison of attitude hardware for observation missions

The science goals of space observation missions have become increasingly demanding in terms of science availability and spacecraft agility requirements. A non-exhaustive list of such observation missions with individual requirements is presented in Table 1. They are listed in chronological order of launch year, and the following acronyms are used if needed: Atmospheric Remote-sensing Infrared Exoplanet Large-survey (ARIEL), Advanced Telescope for High-ENergy Astrophysics (ATHENA), Hubble Space Telescope (HST), James Webb Space Telescope (JWST), Solar Dynamics Observatory (SDO), Solar Orbiter (SolO), and XMM-Newton (XMM). In the table, the X_B-axis refers to the Sun direction from the spacecraft point of view, the Y_B-axis to the spacecraft transverse axis, and the Z_B-axis completes the right-handed orthogonal triad (for most of the missions, Y_B corresponds to the solar array axis and Z_B to the spacecraft longitudinal/optical axis).

Table 1: Space observation missions: requirements, attitude constraints, and spacecraft mass and inertia properties

Mission, Launch year	Science avail.	Slew Rate [°/min]	Attitude Constraints	Mass [kg]	Moment of Inertia [kg.m^2]
HST, 1990	90%[7]	6[7]	Depends on position on orbit and target: from X_BZ_B-plane[7]	11,110	$\begin{bmatrix}31,046 & & \\ & 77,217 & \\ & & 78,754\end{bmatrix}$[27]
Cassini, 1997	-	X_B & Y_B: 7.8[11] Z_B: 15.6	Two Sun "keep-out zones"[11]	5,570	$\begin{bmatrix}8,970 & & \\ & 9,230 & \\ & & 3,830\end{bmatrix}$[43]
XMM, 1999	-	1.5[9]	X_B: free[38] Y_B: ±20° Z_B: ±20°	3,800	-
SDO, 2010	95%[32]	Calib.: 18[39]	X_B: free[36] Y_B: ±2.5° Z_B: ±2.5°	3,000	$\begin{bmatrix}1,923 & 45 & -4 \\ 45 & 3,640 & -5 \\ -4 & -5 & 3,000\end{bmatrix}$[35]
SolO, 2020	-	Calib: 6[42]	X_B: free Maximum off-pointing from Sun line: ±6.5°[12]	1,800	-
JWST, 2021	70%[1]	1.6[25]	X_B: free[33] Y_B: [-53; 0]° Z_B: ±5°	6,200	$\begin{bmatrix}67,946 & -83 & 11,129 \\ -83 & 90,061 & 103 \\ 11,129 & 103 & 45,821\end{bmatrix}$[25]
ARIEL, 2029	85%[8] (exp. 90-92%)	4.5[26]	X_B: free[8] Y_B: ±30° Z_B: ±6.75°	1,500	-
ATHENA, 2035	90%[3]	Nominal: 1[2] Opp. target: 4[3]	X_B: free[3] Y_B: ±34° Z_B: ±5°	8,000	$\begin{bmatrix}200,000 & & \\ & 220,000 & \\ & & 20,000\end{bmatrix}$[10]

DOI: 10.13009/EUCASS2022-6149

These industrial technical concepts impose several attitude guidance challenges to satisfy the missions' objectives. For all of them, attitude exclusion zones are hard constraints, whose violation would lead to the loss of the missions. For HST, XMM, JWST, ARIEL, and ATHENA, the attitude constraints are due to the high sensitivity of the scientific instruments, and the necessity to prevent sunlight from entering their field of view. Concerning SDO and SolO, both shall remain Sun-pointing throughout most of the missions to stay within their thermal limits and for the Sun-observing instruments to take continuous measurements.[12,36] During calibration maneuvers they must keep the guide telescopes' field of view well outside a Sun exclusion zone.[36] Moreover, all the aforementioned missions aim to improve scientific return by maximizing the image quality and resolution. This is achieved by augmenting the telescope's objective aperture and area, and thus its focal length. This leads to designing massive space observatories (see individual mass and inertia properties in Table 1).

In addition, the overall science availability is expected to be more than 85% for most of the reviewed missions. To maximize the time availability for science observations, it is important to reduce the time spent reorienting the spacecraft. One of the main levers to achieve this reduction is to focus on the slew maneuvers between observations. Reaction-wheels are well-fitting to this task: they can store rotational energy by conserving angular momentum and provide stability and counteract external disturbances by exchanging momentum with the satellite body. Thus, they can provide high pointing accuracy and agility, and in addition can be used for reorienting the spacecraft between observations as well as precisely holding its attitude during the science mode. The benefit of using reaction wheels over thrusters for re-orientation maneuvers (while orbiting) is that there is no need to use any fuel. The optimal attitude actuation of such massive spacecraft is not a trivial issue when there is no large computational power on-board to perform convex optimization online. The actuation shall use at best the spacecraft agility and avoid exciting structural modes since the steady-state shall be reached as fast as possible. The attitude maneuver performances are directly driven by the attitude actuator constraints. The reaction wheels limitations are their maximal torque and angular momentum capacities about their rotation axis. A typical RW-configuration is the symmetric pyramidal arrangement as it enables to provide momentum capacity and torque in each of the three spacecraft axes and thus to ensure a three-axis pointing capability while being robust to any reaction wheel failure. Fixed in the body-frame, the reaction wheels are usually set up about the axis where the maximum momentum capacity is required for slew maneuvers. The reaction wheel equipment characteristics associated to the previous listed missions are presented in Table 2. SolO and ARIEL possess four reaction wheels,[4,12] but no further information could be found on their configuration and characteristics.

Table 2: Space observation missions: spacecraft reaction wheels characteristics

Mission, Ref.	No. of RWs	RWs spatial configuration	RWs spin axes direction	Nominal Ang. Mom. [Nms]	Nominal Torque [mNm]	$K_{T\to h}$ ratio (see Eq. 2) [s]
HST [18]	4	Symmetrical pyramid	Elevation angle: 45° Spacing angle: 20°	250	820	305
Cassini [11,20,23]	3 +1	Regular pyramid Back-up, steerable	Elevation angle: 54°	34	160	213
XMM [29,30]	4	Symmetrical pyramid	Separation angles: - Elevation plane: 60° - Azimuth plane: 120°	40-45	211 (248-37 max. loss torque)	190-213
SDO [21,36]	4	Regular pyramid	Elevation angle: 30°	70	250	280
JWST [14,19]	6	Regular pyramid	Elevation angle: 45°	68	55 (75-20 max. loss torque)	1236
ATHENA [3,10]	5	Regular pyramid	Elevation angle: 40°	68	55 (75-20 max. loss torque)	1236

To further improve the scientific performance, more and more space observatories are MB/MA spacecraft that possess several on-board instruments sharing one larger common mirror (instead of unmoving instruments sharing individually or in parallel the same light focused by one or several unmoving mirrors like HST[7] or XMM[22]). Examples are the recently launched JWST, as well as the planned ATHENA and ARIEL telescopes. Both JWST and ATHENA are composed of a main body and a large movable primary mirror mounted on a hexapod mechanism.[3,7] For ARIEL,

DOI: 10.13009/EUCASS2022-6149

a short-range fine steering mechanism enables to change the focus of the secondary mirror.[5] The repointing maneuver of such spacecraft involves a slew maneuver performed with reaction wheels, and a mirror steering towards the line of sight of the observing instrument. In the case of large moving mirrors, the spacecraft attitude can change significantly when the mirror is moved. When the target attitude is only known shortly before slewing the spacecraft and the observation is time-critical, knowing and updating in real-time the spacecraft attitude after the mirror motion enables to save time since the closed-loop control system does not have to correct the attitude error induced by the mirror motion. Therefore, an autonomous computation of the repointing maneuver in the guidance strategy is an asset for such missions.

2.2 Benchmark mission and guidance problem

Driven by the examples from section 2.1, a benchmark observation spacecraft was defined by Airbus, and is introduced and schematically represented on Figure 1. It is a MB/MA space telescope with a large primary mirror (in blue). The mirror is fixed on an articulated six degree-of-freedom mechanism (in green). To discuss the attitude guidance problem, it is useful to define an attitude reference frame, and a coordinate system that is fixed to the spacecraft. The observation targets are defined in the attitude reference frame {R}. The axes are defined as follows: x_R is parallel to the Sun-spacecraft line where the spacecraft is the mirror node to instrument focal plane, pointing away from the Sun, y_R is the transverse axis, orthogonal to the Sun-LoS pointing plane and z_R completes the right-handed orthogonal triad.

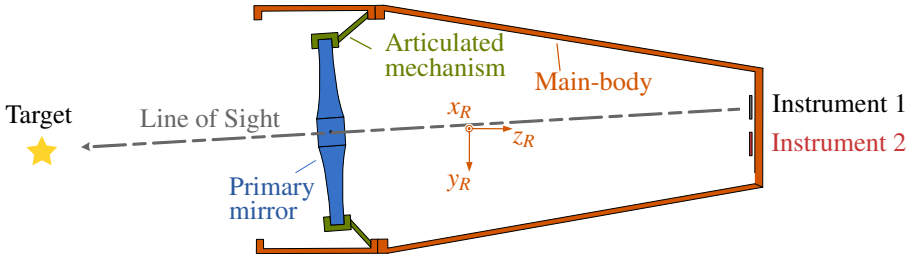

Figure 1: Benchmark MB/MA Spacecraft: line-of-sight direction and attitude reference frame

The body-fixed reference frame {B} consists of three orthogonal axes and has its origin at the spacecraft center of mass. The Z_B-axis is defined such that $-Z_B$ points in the same direction as the LoS, along the mirror perpendicular axis at its neutral position. The attitude is defined as the orientation of the coordinate frame {B} w.r.t the attitude reference frame {R}. In this article, the corresponding attitude angles are defined by the Tait-Bryan rotation sequence about the x-y-z axes: ϕ is the angle about x_R, θ is the angle about the rotated y-axis, and ψ is the angle about the twice rotated z-axis, i.e. $T_{BR} = T_3(\psi)T_2(\theta)T_1(\phi)$.

Repointing the spacecraft between two observations involves an actuation of the articulated mechanism (to steer the mirror towards the instrument used for the next observation) followed by a spacecraft slew maneuver (to change the spacecraft attitude such that the LoS points towards the new target). The repointing guidance problem is derived from the requirements identified in the previous section. It consists in performing autonomous repointing maneuvers from one attitude to another, under safety critical attitude constraints. The line-of-sight allowed pointing zone is conveniently expressed in this reference frame since the X_R-axis is aligned with the Sun-spacecraft line. The attitude constraints for the benchmark mission are based on the ones from the XMM-Newton, JWST, ARIEL and ATHENA missions. The rotation about the X_B-axis is unconstrained. In order to prevent sunlight from entering the instruments' field of view, the LoS should stay within ±35° about the Y_B-axis and should not rotate about the Z_B-axis. As there is no rotation around Z_B-axis, the azimuth and elevation angles can be directly transposed into Euler angles as follows: ϕ corresponds to the azimuth angle, θ corresponds to the elevation angle and ψ is 0 in the considered case.

Moreover, the spacecraft should perform the repointing maneuvers (i.e. mirror motion plus spacecraft slew maneuver) by only commanding the target quaternion with no other information from ground. Thus, the motion planning algorithms should be computationally efficient and run on-board in finite time. This is challenging as the guidance generation problem is almost always nonconvex, which typically means that convex optimization is not an efficient and reliable on-board solution yet, and no other solution is available in the literature to the best knowledge of the authors. For this benchmark mission, the mirror motion is assumed to be performed in open loop, prior to the spacecraft slew. A pointing control architecture based on the one proposed in the investigation of MB/MA methods[34] is used. It enables an autonomous LoS guidance and control of a MB/MA spacecraft with an active moving mirror. A reference repointing maneuver is used to compare the performance of the different guidance solutions. It consists in

DOI: 10.13009/EUCASS2022-6149

guiding the LoS azimuth and elevation angles from (0°,30°) to (120°,20°).

2.3 Spacecraft torque and angular momentum capacity

The spacecraft angular momentum capacity and torque capacity depend on the individual reaction wheels characteristics (i.e. maximal torque and angular momentum about their rotation axis) and on the reaction wheel array architecture (i.e. the orientation of the reaction wheels). For the present study, and based on the comparison of the reaction wheels equipment from section 2.1, a configuration of five identical active reaction wheels is considered. They are accommodated in a pyramidal configuration such that the base of the pyramid forms a regular pentagon. Considering the guidance problem, the reaction wheels configuration must allow to perform sky observations (with line-of-sight along the Z_B-axis) while satisfying the guidance constraints (i.e. with constraints for rotations around the Y_B-axis). The configuration should also enable to compensate the solar torque induced angular momentum accumulation about to the Y_B-axis. Thus, the reaction wheels rotation axes are chosen at a specific opening angle α from the Y_BZ_B-plane and distributed equally with an angle β between the subsequent edges of the lateral faces. The torque and angular momentum from each reaction wheel are mapped into body frame torque and angular momentum through the reaction wheel transformation matrix $A_{RW\to B}$.

$$A_{RW\to B} = \begin{bmatrix} \sin(\alpha) & \sin(\alpha) & \sin(\alpha) & \sin(\alpha) & \sin(\alpha) \\ 0 & \sin(\beta)\cos(\alpha) & \sin(2\beta)\cos(\alpha) & \sin(3\beta)\cos(\alpha) & \sin(4\beta)\cos(\alpha) \\ \cos(\alpha) & \cos(\beta)\cos(\alpha) & \cos(2\beta)\cos(\alpha) & \cos(3\beta)\cos(\alpha) & \cos(4\beta)\cos(\alpha) \end{bmatrix} \tag{1}$$

A way to visualize the spacecraft angular momentum and torque capacity is obtained by drawing the so-called angular momentum and torque envelopes, which represent the maximum available angular momentum and torque in any direction. It consists in projecting the available torque and angular momentum of each reaction-wheel into the three dimensional body-space. The algorithm presented by Markley et al[24] has been used to create a function that computes and draws the envelopes. Depending on whether the torque or the angular momentum envelope is considered, each facet represents a saturated command in torque or angular momentum of all wheels but two: all the wheels are actuated at their maximum value except the two being parallel to the facet. In the same manner, each edge represents a saturated command of all wheels except the one being parallel to that same edge.

In the case of reaction wheels, the torques and angular momentum envelopes have the same shape, and a ratio $K_{T\to h}$ between both envelopes can be defined. In the case of identical reaction wheels, the reaction wheel configuration does not impact this ratio: it is equal to the ratio between the allocated angular momentum and torque for the guidance. It only depends on the individual reaction wheel maximum angular momentum ($h_{max,RW}$) and torque ($T_{max,RW}$) - like the ones provided in Table 2, and their respective feedforward guidance allocation rates (α_h and α_T).

$$K_{T\to h} = \frac{\alpha_h \cdot h_{max,RW}}{\alpha_T \cdot T_{max,RW}} \tag{2}$$

This being said, it is possible in this case to draw a reaction-wheel envelope scaled to the maximum torque capability of a single wheel as done by Markley et al[24] (see Figure 2). It is highlighted that multiplying the reaction-wheel envelope by the angular momentum capacity allocated for the slews will provide the angular momentum envelope, while multiplying it by the torque capacity allocated for the slews will provide the torque envelope for the guidance.

The allocated torque and angular momentum for the slew maneuver guidance enables to keep a portion of the global angular momentum storage capability and torque capacity for feedback control during the maneuver. Moreover, an additional part of the global angular momentum storage capability is reserved for momentum accumulation, which is mainly caused by the solar radiation pressure disturbing torque for most of the space observation missions. For this reason, it is very likely that a slew maneuver starts with a non-zero angular momentum storage. This initial condition must be considered when building the angular momentum envelope. Instead of attributing the maximum angular momentum capacity C_i to each facet as in Markley's algorithm,[24] a current available capacity h_i is computed where the initial angular momentum is subtracted from the maximal one. To do so, for each facet i of the envelope, the initial angular momentum ($\mathbf{h}_0$) is projected on the facet's normal unit vector ($\mathbf{n}_i$) and subtracted from its maximum angular momentum capacity $\mathbf{C}_i$ (see Eq. 3). The case $h_i > C_i$ is possible, i.e. angular momentum bias may increase agility for some maneuvers.

$$h_i = C_i - (\mathbf{h}_0 \cdot \mathbf{n}_i) \tag{3}$$

Thanks to the geometric properties of the envelopes constructed in the proposed form, it is possible to perform analytical checks by computing the distance ratio between the vector and the envelope in order to verify if a vector of

DOI: 10.13009/EUCASS2022-6149

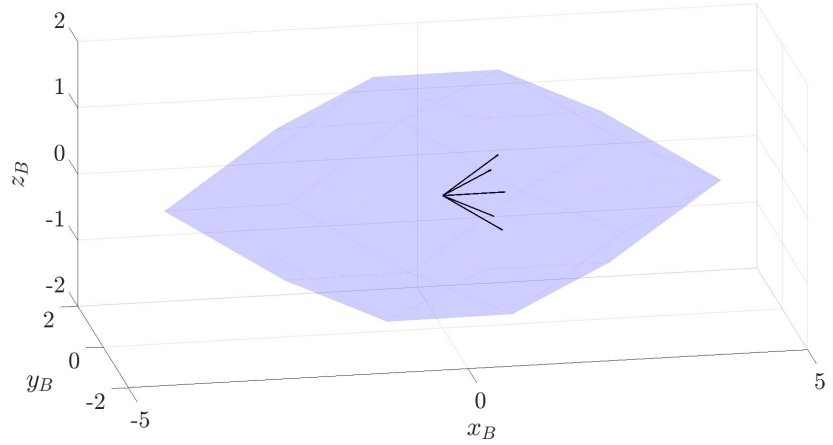

Figure 2: Unit envelope for the considered RW configuration and characteristics

interest is within the envelope, on its limit, or violating it. The method is derived for the angular momentum envelope, but the same checks can be done with the torque envelope.

For all the facets of the angular momentum envelope, the unit vector of interest $\mathbf{v}$ is projected on the normal unit vector ($\mathbf{n}_i$) of each facet i:

$$\mathbf{p}_{\mathbf{n}_i}(\mathbf{v}) = (\mathbf{v} \cdot \mathbf{n}_i)\, \mathbf{n}_i \tag{4}$$

Moreover, each facet i is at the maximum capacity distance $\mathbf{C}_i$ from the center. Thus, dividing each projected vector length by this maximum capacity will provide the distance ratio r_i between the projected vector on facet i and the facet i maximum capacity:

$$r_{h_i} = \frac{\|\mathbf{p}_{\mathbf{n}_i}(\mathbf{v})\|}{h_i} \tag{5}$$

The highest ratio r_i over all facets i represents the multiplying factor by which the input vector needs to be divided to exactly reach the angular momentum envelope:

$$r_h = \max_{i \in [\![1;N_{facets}]\!]} r_i \tag{6}$$

This ratio r can be seen as a angular momentum norm,[15] whose value leads to the following useful property 7.

$$\begin{cases} r_h < 1 \Leftrightarrow \mathbf{v} \text{ is inside the angular momentum envelope} \\ r_h = 1 \Leftrightarrow \mathbf{v} \text{ reaches the angular momentum envelope} \\ r_h > 1 \Leftrightarrow \mathbf{v} \text{ crosses the angular momentum envelope} \end{cases} \tag{7}$$

This ratio can be used for checking the violation/margin of an input vector, or it can be used to find the maximum torque and angular momentum capacities about a direction of interest. This will be used in section 4.1 to compute optimal maneuver times.

3. Reference axis-by-axis maneuver guidance

As mentioned in the guidance problem definition in section 2, a repointing phase is composed of a mirror motion followed by a spacecraft slew maneuver. A typical industrial approach, paradigmatic of the state-of-practice, to perform a slew maneuver under attitude constraints consists in dividing the multi-axis maneuver into out-of-plane and in-plane single-axis maneuvers of the telescope line of sight.[16,17,28] For example, using the $y_R z_R$-plane from Figure 1, which is defined by its Sun-pointing normal, ensures that the attitude constraints for Sun avoidance are explicitly considered. In this case, a first rotation around the $\mathrm{Y_B}$-axis of the spacecraft body frame cancels the initial elevation angle by bringing the spacecraft boresight into the azimuth plane. Then, a second rotation is performed around the $\mathrm{X_B}$-axis

DOI: 10.13009/EUCASS2022-6149

(azimuth), which will rotate the spacecraft boresight within the azimuth plane, and finally a third rotation around the Y_B-axis to lead the spacecraft boresight out of the azimuth plane to the new elevation angle at the final line-of-sight direction. As explained in section 2.3, different sub-maneuvers are generated depending on the available angular momentum. The envelope-constraint guided torque for the reference repointing maneuver is presented in Figure 3 using normalized time (x-axis) and torque (y-axis) values to respect confidentiality constraints from the industrial partner. It is composed of a first bang-bang sub-maneuver about the Y_B-axis (from 0.12 to 0.38 in the normalized time axis), a second bang-coast-bang maneuver about the X_B-axis (from 0.38 to 0.76 in the normalized time axis) and a third bang-bang maneuver about the Y_B-axis (from 0.76 to 0.98 in the normalized time axis). The corresponding closed-loop time response obtained using a high-fidelity, nonlinear simulator provided by Airbus is shown on Figure 4. The slew maneuver components (named as SC Man. 1, 2, 3 in the figure) performed after the mirror motion ensure that the attitude constraints for Sun avoidance are explicitly considered.

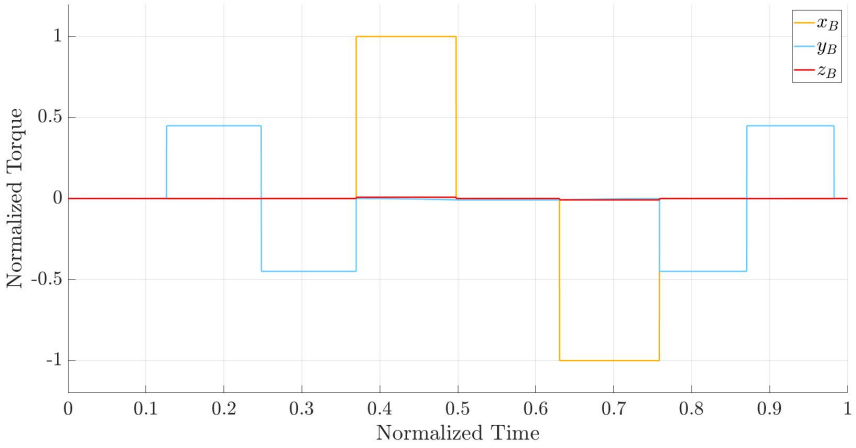

Figure 3: Commanded torque from axis-by-axis guidance in {B}-frame w.r.t {R}-frame

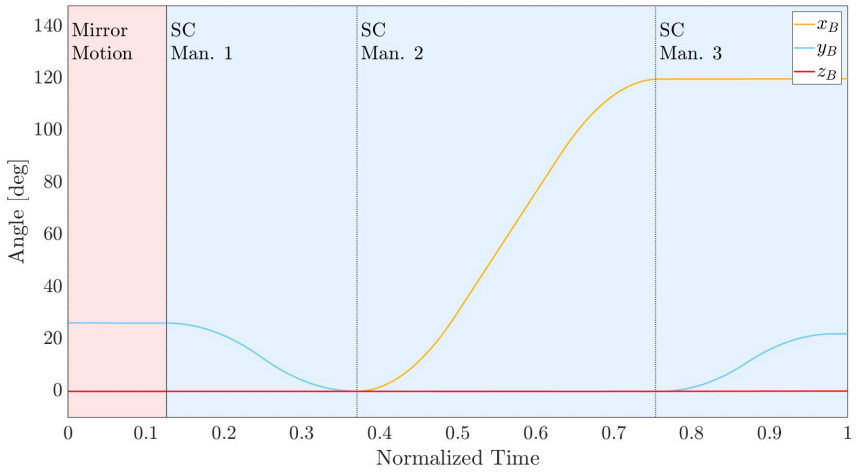

Figure 4: S/C Euler Angles from axis-by-axis guidance in {B}-frame w.r.t {R}-frame

A very important aspect in any project is the visualization of the gains. In order to compare the maneuver times between the different slew maneuvers, a pixel map is proposed (see Figure 5). Starting from extreme initial angles in body-frame (azimuth: -180°, elevation: -35°), the map covers the whole set of allowed final angles. Each pixel corresponds to a normalized maneuver time w.r.t. the maximal maneuver time for the covered azimuth (X_B-axis) and elevation ranges (Y_B-axis). The map represents a maximum azimuth range of 180°, as the spacecraft can be rotated without constraint around the X_B-axis, leading to a maximum rotation of 180°. On the other hand, time-map is

DOI: 10.13009/EUCASS2022-6149

symmetrical about the Y_B-axis because of the three consecutive generated maneuvers. As for the previous figure, the maneuver times have been normalized, the right vertical bar.

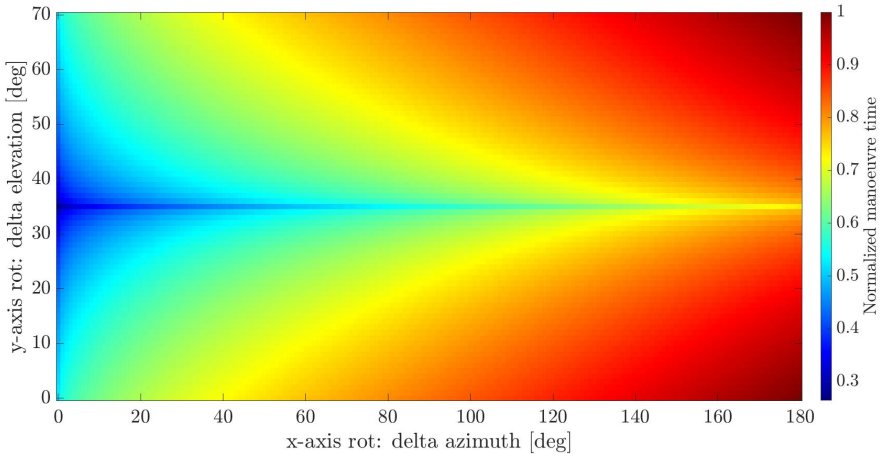

Figure 5: Maneuver time pixel map for the envelope-constrained axis-by-axis guidance

4. Novel coupled-axis guidance

The previous axis-by-axis guidance approach is a robust solution that enables to satisfy the environment constraints while being easy to implement on-board and capable of operating autonomously. Indeed, the entire torque and angular momentum available about the individual X_B and Y_B-axes in the body-frame can be used since only one axis is used per slew maneuver. To do so, the maximum angular momentum and torque about these two axes of interest are computed using the envelopes geometric properties from section 2.3. However, this approach is not the most time efficient since three consecutive sub-maneuvers (and thus six acceleration and deceleration phases) are performed for each slew maneuver. Thus, a novel coupled-axis guidance solution requiring only one acceleration and one deceleration phase, and satisfying the attitude requirements, is proposed in this section. For any given slew maneuver, the optimal maneuver time is retrieved from the spacecraft envelopes, and the slew profile is computed analytically. Both approaches, the reference single-axis and the proposed coupled-axis one, are finally compared.

4.1 Optimal maneuver time computation

This section presents the method to compute the optimal maneuver time for any slew angle to cover $\mathbf{\Delta}_{angle}$. Starting from this slew angle, the minimal actuation time, i.e. using all the available torque and disregarding the angular momentum limitation, is first computed. Then it is checked whether actuating the spacecraft during this minimal time at maximum torque leads to a violation of the available angular momentum. Section 4.1.1 and section 4.1.2 handle respectively the cases without and with violation and provide the corresponding optimal maneuver times.

The slew angle $\mathbf{\Delta}_{angle}$ counterpart in the momentum domain is noted $\mathbf{\Delta}_p$ and is computed as in Eq. 8. This quantity is not physically meaningful but will be helpful since the angular momentum and torque envelopes are already available.

$$\mathbf{\Delta}_p = \mathcal{J}_{SC} \cdot \mathbf{\Delta}_{angle} \tag{8}$$

Let us consider the ratio $K_{T\to\mathbf{\Delta}_p}$ by which the vector $\mathbf{\Delta}_p$ needs to be multiplied so that it reaches the torque envelope. This ratio corresponds to the ratio r from 7 when the method is applied to the input vector $\mathbf{\Delta}_p$ and the torque envelope. This ratio is of unit s^2 and its the square root represents the actuation time to cover $\mathbf{\Delta}_{angle}$ at maximum torque.

$$t_{min} = \sqrt{K_{T\to\mathbf{\Delta}_p}} \tag{9}$$

Now it needs to be checked whether actuating the reaction wheels during this time t_{min} at maximum torque leads to an angular momentum violation. As explained in section 2.3, the ratio $K_{T\to h}$ between the torque and angular momentum envelopes is known and fixed. It can be seen as a performance indicator, representing the time required

DOI: 10.13009/EUCASS2022-6149

to reach the maximum angular momentum when actuating at the maximum torque. Thus, comparing the optimal time t_{min} to the ratio $K_{T\to h}$ enables to check whether the angular momentum is violated for the maneuver to perform.

4.1.1 Optimal maneuver time without angular momentum violation

In the case $\boldsymbol{t_{min} < K_{T\to h}}$, actuating the spacecraft at maximum torque during t_{min} will not lead to any angular momentum violation. In practice, a bang-bang maneuver can be performed, which means that the spacecraft can be accelerated (first bang phase) and decelerated (second bang phase) at maximum acceleration without necessarily reaching the maximum angular rates. In this case, the optimal maneuver time is directly deduced from the minimal actuation time as follows:

$$t_{man} = 2 \cdot t_{min} \tag{10}$$

4.1.2 Optimal maneuver time with angular momentum violation

In the case $\boldsymbol{t_{min} > K_{T\to h}}$, the maximum angular momentum is reached if the spacecraft is actuated at maximum torque during t_{min}. The spacecraft can be only actuated at maximum torque during $K_{T\to h}$, which is not enough to reach $\boldsymbol{\Delta}_p$, and thus cover the slew angle $\boldsymbol{\Delta}_{angle}$. The missing time to reach $\boldsymbol{\Delta}_p$ is the time needed to reach $\boldsymbol{\Delta}_p$ at maximum angular momentum. This corresponds to the time ratio $K_{h\to\boldsymbol{\Delta}_p}$ between $\boldsymbol{\Delta}_p$ and the angular momentum envelope. It is computed using the method from section 2.3 and corresponds to the ratio r from 7 when the method is applied to the input vector $\boldsymbol{\Delta}_p$ and the angular momentum envelope. Unlike the ratio $K_{T\to h}$, $K_{h\to\boldsymbol{\Delta}_p}$ depends on the reaction wheels configuration and the maneuver to perform. It represents the minimum time to reach the angular momentum envelope in $\boldsymbol{\Delta}_p$ direction, and it will be different for each maneuver. In this case, the maneuver time will be the sum of the time needed to reach the maximum angular momentum at maximum torque, and the remaining time needed to reach at maximum angular momentum, i.e.:

$$t_{man} = K_{T\to h} + K_{h\to\boldsymbol{\Delta}_p} \tag{11}$$

In practice, more actuation time than t_{min} is needed to reach the expected attitude without violating the maximum angular momentum limit. This means that the spacecraft is first actuated at maximum torque until reaching the angular momentum limit. Then it will be slewed at constant (and maximum) angular momentum during the coasting time, before being decelerated at maximum torque until achieving the desired attitude. Such a maneuver is called bang-coast-bang maneuver.

In both cases, the optimal maneuver times are now known, but the slew angles guidance profiles satisfying the attitude constraints are still missing. This will be the purpose of next section, where the torque-limited (bang-bang torque profile) and angular momentum-limited (bang-coast-bang torque profile) maneuver computations will be derived.

4.2 Analytical guidance profile computation

The proposed guidance principle is to generate a continuous path that enables to slew from permissible initial angles to permissible final angles while satisfying the guidance constraints at each time step.

First, a restricted zone made of the azimuth and elevation angles can be defined. As explained in the guidance problem in Section 2.2, for the considered case there is no restriction in the rotation around X_B-axis, but there is a restriction of ±35° around the Y_B-axis. Further, rotation around Z_B-axis is not allowed. From these azimuth/elevation restrictions the following permissible zones can be defined: in the orthogonal coordinate system made by the X_B-axis and the Y_B-axis, the permissible zone is a rectangle spanning ±180° on the X_B-axis and ±35° on the Y_B-axis. This permissible zone is a topological space. Hereafter are some definitions:

- By definition, a convex region is a region where any line segment joining any two points from the region entirely lies within the region, i.e. every point on the line segment is also within the region.[37]
- A path from a point x to a point y in a topological space X is a continuous function f from the unit interval $[0; 1]$ to X with $f(0) = x$ and $f(1) = y$. The space X is said to be path-connected if any two points in X are connected in X by a path. (A path can be drawn between any two points in the space).[40]
- A convex set is a path-connected space.

DOI: 10.13009/EUCASS2022-6149

Based on the above, it can be concluded that the permissible zone is convex, and thus a connected space. This means that it is possible to draw a path from any point situated in the restricted zone to any other point in the same zone. Therefore, it will be possible to find a slew maneuver from any initial Euler angles (with the subscript i) in the zone to any final Euler angles (with subscript f) in the zone, within this zone:

$$\begin{cases} (\phi_i \;\; \theta_i \;\; \psi_i) & = (\text{azimuth}_i \;\; \text{elevation}_i \;\; 0) \\ (\phi_f \;\; \theta_f \;\; \psi_f) & = (\text{azimuth}_f \;\; \text{elevation}_f \;\; 0) \end{cases} \tag{12}$$

Since a rest-to-rest maneuver starts and ends with no velocity, the corresponding initial and final Euler rates are zero. This implies that the acceleration and deceleration must be performed using the same amount of time. For each slew maneuver, the optimal maneuver time has been computed from the angular momentum and torque envelopes in section 4.1. In the end, this introduction has proven that a slew maneuver guidance profile combining the x- and y- axes can be generated. The torque-limited and angular momentum-limited profiles are respectively computed in sections 4.2.1 and 4.2.2.

4.2.1 Torque-limited maneuver profile

This section presents the case from section 4.1.1 where the angular momentum is not violated, and thus a bang-bang torque profile can be generated. It consists in accelerating and decelerating the spacecraft about the first two Euler axes simultaneously. In order to generate the Euler angles profiles for the maneuver, the available acceleration about the first two Euler axes is needed. The available torque T_{max} in the $\mathbf{\Delta}_p$ direction is computed using the envelope geometry from section 2.3, and the available acceleration is computed from the available torque as follows:

$$\boldsymbol{\alpha} = \boldsymbol{J}_{SC}^{-1} \cdot \boldsymbol{T}_{max} \tag{13}$$

The slew angle vector Δ_{angle} to cover during the maneuver is the difference between the final and initial Euler angles:

$$\mathbf{\Delta}_{angle} = \begin{bmatrix} \phi_f - \phi_i \\ \theta_f - \theta_i \\ 0 \end{bmatrix} \tag{14}$$

Thus, considering that the available acceleration is

$$\boldsymbol{\alpha} = \begin{bmatrix} \alpha_\phi \\ \alpha_\theta \\ \alpha_\psi \end{bmatrix}, \tag{15}$$

the acceleration times per Euler axis are t_θ and t_ϕ can be computed from the individual available accelerations per Euler axis as follows:

$$t_\phi = \sqrt{\frac{\phi_f - \phi_i}{\alpha_\phi}} \quad ; \quad t_\theta = \sqrt{\frac{\theta_f - \theta_i}{\alpha_\theta}} \tag{16}$$

The optimal time t_{min} computed in eq. 9 is actually the biggest time between t_θ and t_ϕ. Indeed, it corresponds to the biggest ratio among the three axes between the available torque T_{max} and the $\mathbf{\Delta}_p$ direction.

As an example, the case $t_\theta < t_\phi$ is considered, (but it is noted that it is the same reasoning for $t_\phi < t_\theta$). In this example, the acceleration time for the maneuver is $t_{min} = t_\phi$. This means that the acceleration about the y-axis that is going to be used for the maneuver will be lower than the available one for the y-axis, since more time is available to perform the y-axis Euler rotation. The scaled acceleration about the y-axis is computed as follows:

$$\alpha_{\theta,\text{scaled}} = \frac{\theta_f - \theta_i}{{t_\phi}^2} = \alpha_\phi \frac{\theta_f - \theta_i}{\phi_f - \phi_i} \tag{17}$$

By integrating the accelerations twice, and considering that the initial and final velocities are zero (rest-to-rest maneuver) as well as the continuity of $\theta(t)$ at $t = t_{min}$, the expression of θ in function of the time during the maneuver can be expressed.

$$\phi(t) = \begin{cases} \phi_i + \alpha_\phi \cdot \dfrac{t^2}{2} & \forall t \in [0; t_{min}] \\ \phi_i - \alpha_\phi \cdot {t_\phi}^2 + 2\alpha_\phi \cdot t_\phi \cdot t - \alpha_\phi \cdot \dfrac{t^2}{2} & \forall t \in [t_{min}; 2t_{min}] \end{cases} \tag{18}$$

DOI: 10.13009/EUCASS2022-6149

The same profile is valid for the θ angle, using $\alpha_{\theta,\text{scaled}}$ instead of α_θ as acceleration about the y-axis.
In the same manner, if $t_\phi < t_\theta$, then $t_{min} = t_\theta$ and the scaled acceleration about the x-axis is:

$$\alpha_{\phi,\text{scaled}} = \alpha_\theta \cdot \frac{\phi_f - \phi_i}{\theta_f - \theta_i} \tag{19}$$

4.2.2 Angular momentum-limited maneuver profile

This section presents the case where the angular momentum is violated in case of a bang-bang maneuver. To satisfy the angular momentum constraint defined by the momentum envelope, the time of the acceleration and deceleration phases must be reduced to accumulate less angular momentum than the maximum one.

As presented in section 4.1.2, the spacecraft can be accelerated and decelerated at maximum torque during the maximum time $K_{T\to h}$ before reaching the maximum angular momentum value. Then, the coasting time $K_{h\to\mathbf{\Delta}_p}$ is the remaining time to reach $\mathbf{\Delta}_P$ at maximum angular momentum.

Thus, the two bang phases (acceleration and deceleration phases) can last a maximum time of $t_{bang} = K_{T\to h}/2$, and the coast time will last $t_{coast} = K_{h\to\mathbf{\Delta}_p}$.

The guidance formulas from 4.2.1 are extended to compute the coast time analytically. The new acceleration profile will be integrated twice to retrieve the new velocity and angle profiles. The initial and final conditions are unchanged. The coast-phase, lasting t_{coast}, corresponds to a null-acceleration and a velocity plateau. For easier reading, the intervals will be renamed as hereafter:

$$\begin{cases} \mathrm{I}^1_{bang} = [0; t_{bang}] \\ \mathrm{I}_{coast} = [t_{bang}; t_{bang} + t_{coast}] \\ \mathrm{I}^2_{bang} = [t_{bang} + t_{coast}; 2t_{bang} + t_{coast}] \end{cases} \tag{20}$$

Augmented with the coast phase, the acceleration about the x-axis is now expressed as in Eq. 21.

$$\ddot{\phi}(t) = \begin{cases} +\alpha_\phi & \forall t \in \mathrm{I}^1_{bang} \\ 0 & \forall t \in \mathrm{I}_{coast} \\ -\alpha_\phi & \forall t \in \mathrm{I}^2_{bang} \end{cases} \tag{21}$$

By integrating Eq. 21 twice, and by using the continuity arguments at $t = t_{bang}$ and $t = t_{bang} + t_{coast}$, the angle profile can be expressed as follows:

$$\phi(t) = \begin{cases} \phi_i + \alpha_\phi \cdot t^2/2 & \forall t \in \mathrm{I}^1_{bang} \\ \phi_i - \alpha_\phi \cdot \dfrac{t^2_{bang}}{2} + \alpha_\phi \cdot t_{bang} \cdot t & \forall t \in \mathrm{I}_{coast} \\ \theta_i - \alpha_\phi \cdot \left(t_{bang} \cdot t_{coast} + \dfrac{t^2_{coast}}{2} \right) + \alpha_\phi \cdot t \cdot \left(2t_{bang} + t_{coast} - \dfrac{t}{2} \right) & \forall t \in \mathrm{I}^2_{bang} \end{cases} \tag{22}$$

The same reasoning applies for θ about the y-axis.

4.2.3 Verification and comparison of the results

In the previous two subsections, the bang-bang 4.2.1 and bang-coast-bang 4.2.2 Euler optimal-maneuver profiles were obtained. These profiles consist of Euler accelerations ($\ddot{\phi}\ \ddot{\theta}\ \ddot{\psi}$), rates ($\dot{\phi}\ \dot{\theta}\ \dot{\psi}$), and angles ($\phi\ \theta\ \psi$). For verification and simulation, it is better to use the equivalent spacecraft body angles. The transformation involved using the Euler-to-Body relations[31] to obtain the angular velocity $\boldsymbol{\omega}_B$ and angular acceleration $\dot{\boldsymbol{\omega}}_B$, and the rate and attitude integration of the latter to obtain the body angle as performed by Wertz.[41]

Using the reference maneuver described in Section 3, the proposed coupled-axis guidance is applied and the results presented here in Body-frame using the above transformation process.

Figure 6 shows the resulting normalized torques versus normalized times. Comparing this figure with Figure 3 (resulting from the single-axis guidance), it is seen that the proposed guidance is twice as fast as the single-axis one. It is also seen that the resulting guidance is a simultaneous combination of bang-coast-bang maneuvers about the three body axes.

Figure 7 (the equivalent of Figure 4), shows the resulting time-domain response of the Euler angles from the closed-loop, nonlinear simulation of the coupled-axis guidance.

Finally, for ease of comparison to the single-axis guidance, Figure 8 shows the resulting pixel map obtained with the coupled-axis approach. Comparing it to Figure 5 enables to see the advantages of the latter over the single-axis

DOI: 10.13009/EUCASS2022-6149

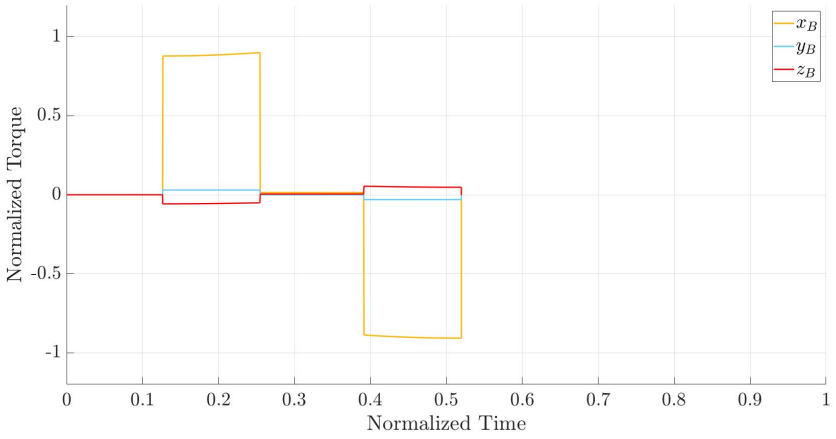

Figure 6: Commanded torque from coupled-axis guidance in {B}-frame w.r.t. {R}-frame

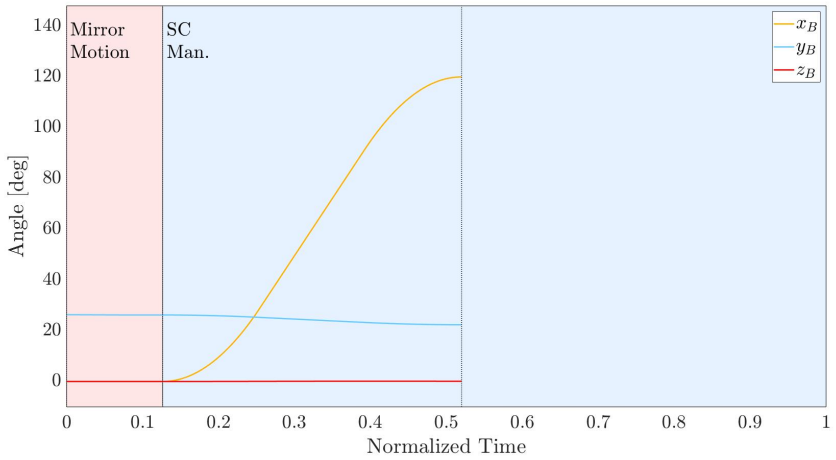

Figure 7: S/C Euler angles from coupled-axis guidance in {B}-frame w.r.t. {R}-frame

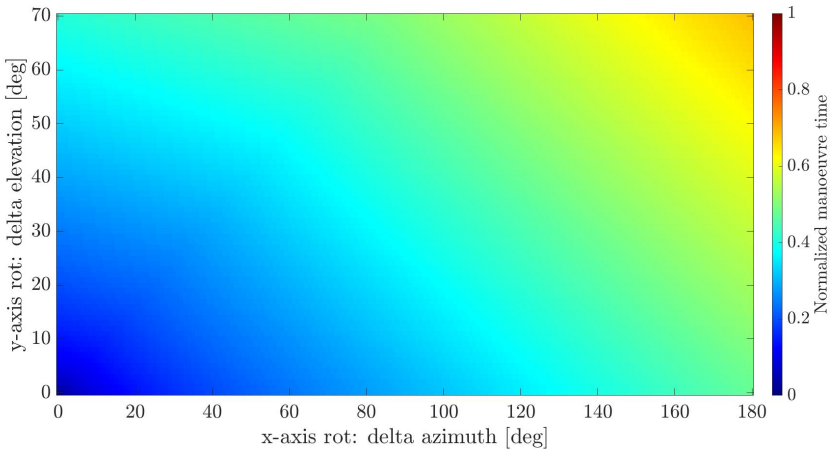

Figure 8: Maneuver time pixel map for the envelope-constrained coupled-axis guidance

DOI: 10.13009/EUCASS2022-6149

guidance. The clear difference comes from the fact that the maneuvers are performed in parallel in the coupled-axis case, and not subsequently.

For a better comparison of the approaches, a pixel map as those in Figures 3 and 4 can be obtained but using for the pixels' colors the ratio between their corresponding normalized maneuver times (see the different colormap legend on the right of the figure). The map on Figure 9 represents the coupled-axis over the axis-by-axis maneuver times. Since the ratio is always lower than one, the maneuver generated from the coupled-axis guidance is always faster than that with the axis-by-axis approach. There is only one maneuver for which the ratio is one, i.e. the coupled-axis maneuver lasts the same time than the axis-by-axis guidance: the case (azimuth: -180°, elevation: -35°) to (azimuth: -180°, elevation: 0°). This makes sense since in this specific case the same maneuver is generated by both methods. It is observed that there are improvements of more than 50% in the maneuver time for almost half of the cases. This corresponds to the zones where the ratio is smaller than 0.5, i.e. the blue-to-green region at the bottom of the map. The average ratio of this test case is 0.55, which means that the maneuver time generated with the coupled-axis guidance is in average 1.8 times faster than the one generated with the axis-by-axis guidance.

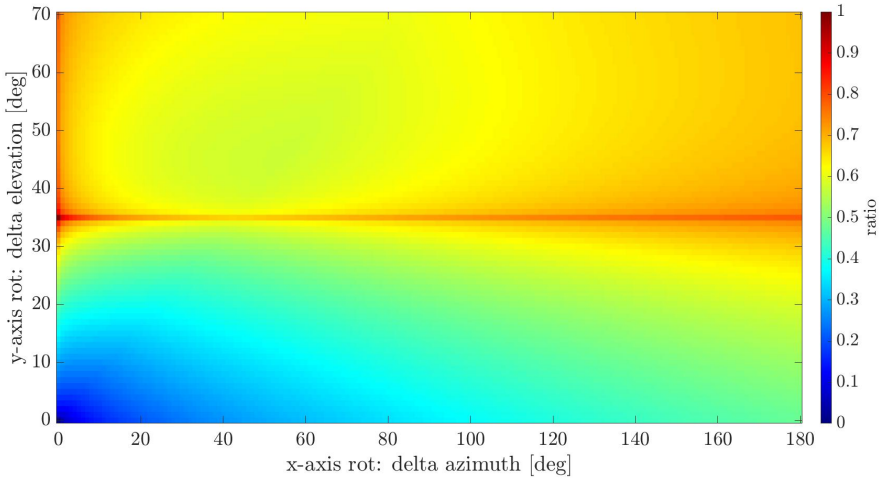

Figure 9: Pixel map of ratio coupled-axis to axis-by-axis maneuver times

Finally, the proposed approach was implemented and assessed by Airbus team in an internal multi-body space telescope observation benchmark. The simulation encompassed all the representative phases' sequencing in such missions: from pure science observation to the different operation/maintenance ones (such as slew maneuvers, reaction wheel off-loading, calibrations,...). Preliminary results indicate that the developed coupled-axis guidance results in an increase of the overall science availability from 89%[13] to 91%, which represents a reduction of more than 20% of the operational time during the mission.

5. Conclusions

In this article, the guidance problem for re-orienting observation spacecraft under safety critical attitude constraints has been studied. A reference guidance based on the industrial state-of-practice for this type of mission was implemented taking into account the spacecraft exact torque and angular momentum capacity. A novel, coupled-axis guidance strategy was developed to minimize maneuver time. It is based on a systematic analytical approach that computes a time-optimal guidance in finite time for a given spacecraft design and set of observation targets.

Results show that the proposed coupled-axis guidance substantially improves the available time for scientific observations. Indeed, it systematically generates faster slew maneuvers than the reference guidance (45% in average, and up to more than 50% for some targets). In the case of multi-body/multi-actuator spacecraft, where the instrument motion can represent between 5-10% of the total mission maneuver time, such a coupled-axis approach could lead to considerable improvement on the time devoted to science. Further, the ease of implementation of the approach means that it satisfies the transparent and clear requirements by industry of any algorithm that must be deployed on-board.

DOI: 10.13009/EUCASS2022-6149

6. Acknowledgments

The results presented in this article are the outcome of the PhD project MACON "Integrated Multi-Actuator CONtrol design for multi-body line-of-sight pointing of space missions". It is conducted at the University Carlos III of Madrid, Spain, funded and supported by Airbus in Friedrichshafen, Germany. The first author gladly acknowledges and thanks for this support.

References

[1] JWST Science Requirements Document. Technical report, NASA, 2006.

[2] ATHENA Assessment Study Report. Technical report, European Space Agency, 2011.

[3] ATHENA CDF Study Report: CDF-150(A). Technical report, European Space Agency, 2014.

[4] ARIEL AOCS, CDF Study IFP. Technical report, ESTEC Concurrent Design Facility Team, ESA, 2015.

[5] Ariel Assessment Study Report. Technical report, European Space Agency, 2017.

[6] ARIEL Payload Design Description. Technical report, ARIEL Payload Consortium, 2017.

[7] Hubble Space Telescope Primer for Cycle 25. Technical report, Space Telescope Science Institute, 2017.

[8] Ariel Definition Study Report. Technical report, European Space Agency, 2020.

[9] XMM-Newton Users Handbook. Technical report, European Space Agency - XMM-Newton SOC, 2021.

[10] ATHENA SC AOCS Concept Report, Iss. 1.4. Technical report, Airbus, 2022.

[11] T. Brown. In-Flight Position Calibration of the Cassini Articulated Reaction Wheel Assembly. In *Guidance, Navigation, and Control Conference*, 2012.

[12] M. Campana, I. Cantiello, G. Monroig, P. Chapman, and S. Strandmoe. AOCS Design for Solar Orbiter, a Mission to just 0.28 A.U. from the Sun. In *ESA GNC 2017*, 05 2017.

[13] F. Pérez Cámara. Extension of the mission timeline simulator with modern optimization capabilities. *MSc thesis, Luleå University of Technology*, 2022.

[14] C. J. Dennehy. A survey of reaction wheel disturbance modeling approaches for spacecraft line-of-sight jitter performance analysis. In *Proc. European Space Mechanisms and Tribology Symp. Munich, Germany*, 2019.

[15] R. Geshnizjani, A. Kornienko, T. Ziegler, J. Löhr, and W. Fichter. Torque Optimal Steering of Control Moment Gyroscopes for Agile Spacecraft. *Journal of Guidance, Control, and Dynamics*, 44(3):629–640, 2021.

[16] H. B. Hablani. Attitude Commands Avoiding Bright Objects and Maintaining Communication with Ground Station. *Journal of Guidance, Control, and Dynamics*, 22(6):759–767, 1999.

[17] J. A Hashmall and L. Mann. Solar Dynamics Observatory High Gain Antenna Handover Planning. In *20th International Symposium on Space Flight Dynamics*, 2007.

[18] S. H. Hur-Diaz, J. H. Wirzburger, and D. Smith. Three Axis Control of the Hubble Space Telescope Using Two Reaction Wheels and Magnetic Torquer Bars for Science Observations. 2008.

[19] M. Karpenko, J. T. King, C. J. Dennehy, and I. M. Ross. Agility Analysis of the James Webb Space Telescope. *Journal of Guidance, Control, and Dynamics*, 42(4):810–821, 2019.

[20] A. Y. Lee and E. K. Wang. In-Flight Performance of Cassini Reaction Wheel Bearing Drag in 1997–2013. *Journal of Spacecraft and Rockets*, 52(2):470–480, 2015.

[21] K. C. Liu, P. Maghami, and C. Blaurock. Reaction wheel disturbance modeling, jitter analysis, and validation tests for solar dynamics observatory. In *AIAA GNC Conference and Exhibit*, page 7232, 2008.

[22] D. H. Lumb, N. Schartel, and F. A. Jansen. X-ray multi-mirror mission (XMM-newton) observatory. *Optical Engineering*, 51(1):011009, feb 2012.

DOI: 10.13009/EUCASS2022-6149

[23] G. A. Macala. Design of the Reaction Wheel Attitude Control System for the Cassini Spacecraft. In *12th AAS/AIAA Space Flight Mechanics Meeting*, 2002.

[24] F. L. Markley, R. G. Reynolds, F. X. Liu, and K. L. Lebsock. Maximum Torque and Momentum Envelopes for Reaction Wheel Arrays. *Journal of Guidance, Control, and Dynamics*, 33(5):1606–1614, 2010.

[25] L. Meza, F. Tung, S. Anandakrishnan, V. Spector, and T. Hyde. Line of Sight Stabilization of James Webb Space Telescope. In *27th Annual AAS Guidance and Control Conference*, 2005.

[26] J. Morales, N. Nakhjiri, J. Colomé, I. Ribas, E. García, D. Moreno, and F. Vilardell. Ariel mission planning. *Experimental Astronomy*, pages 1–23, 01 2022.

[27] G. S. Nurre, J. P. Sharkey, J. D. Nelson, and A. J. Bradley. Preservicing mission - On-orbit modifications to Hubble Space Telescope pointing control system. *Journal of Guidance, Control, and Dynamics*, 18(2):222–229, 1995.

[28] T Ott, S. Goerries, A Schleicher, and S Winkler. AOCS design for the ATHENA X-ray telescope: challenges and solutions. *CEAS Space Journal*, 10(4):519–534, 2018.

[29] M. Pantaleoni. XMM-Newton's operational challenge of changing the attitude control to 4 active reaction wheels, after 12 years of routine operations. In *SpaceOps 2012*, page 1275587, 2012.

[30] M. Pantaleoni, P. Chapman, R. Harris, M. G. Kirsch, R. Kresken, J. Martin, P. McMahon, A. Mcdonald, F. Schmidt, T. Strandberg, et al. Curing XMM-Newton's reaction wheel cage instability: the in-flight re-lubrication experience. In *SpaceOps 2014 Conference*, page 1875, 2014.

[31] J Peraire and S Widnall. Lecture l29-3d rigid body dynamics. *Dynamics*, 2009.

[32] W. Pesnell, B. Thompson, and P. Chamberlin. The Solar Dynamics Observatory (SDO). *Solar Physics*, 275:3–15, 11 2012.

[33] J. Petersen. L2 Station Keeping Maneuver Strategy for the James Webb Space Telescope. In *2019 AAS/AIAA Astrodynamics Specialist Conference*, 2019.

[34] A. Ponche, A. Marcos, T. Ott, and A. Schleicher. Investigation of Multi-Body/Multi-Actuator Modeling Techniques for Applicability to Future Space Observation Missions. In *ESA GNC 2021*, 2021.

[35] S. R. Starin and K. L. Bourkland. Guaranteeing Pointing Performance of the SDO Sun-Pointing Controllers in Light of Nonlinear Effects. In *20th International Symposium on Space Flight Dynamics*, 2007.

[36] S. R. Starin, K. L. Bourkland, K. C. Liu, P. A. Mason, M. F. Vess, S. F. Andrews, and W. M. Morgenstern. Attitude Control System Design for the Solar Dynamics Observatory. In *Flight Mechanics Symposium*, 2005.

[37] R. M. Stark and C. C. Morris. *Finite mathematics: models and applications*. John Wiley & Sons, 2015.

[38] D. Stramaccioni, T. Faust, and J. Hinger. XMM-NEWTON Thermal Design and In-orbit Performance. *SAE Transactions*, 109:499–516, 2000.

[39] M. F. Vess, S. R. Starin, and W. M. Morgenstern. Use of the sdo pointing controllers for instrument calibration maneuvers. 2005.

[40] O. Y. Viro, O. A. Ivanov, N. Y. Netsvetaev, and V.M. Kharlamov. *Elementary topology*. American Mathematical Soc., 2008.

[41] J. R. Wertz. *Spacecraft attitude determination and control*, volume 73. Springer, 2012.

[42] D. Williams. Refresher on Solar Orbiter science planning constraints & process. Technical report, European Space Agency - Solar Orbiter SOC, 2018.

[43] E. Wong and W. Breckenridge. An attitude control design for the Cassini spacecraft. In *Guidance, Navigation, and Control Conference*, 1995.